Electron Shell Ionization of Atoms with Classical, Relativistic Scattering

N. Ekanayake, S. Luo, P. D. Grugan, W. B. Crosby, A. D. Camilo, C. V. McCowan, R. Scalzi, A. Tramontozzi, L. E. Howard, S. J. Wells, C. Mancuso, T. Stanev, M. F. Decamp, and B. C. Walker

Department of Physics and Astronomy, University of Delaware, Newark, Delaware 19716, USA

(Received 14 January 2013; published 15 May 2013)

We investigate forward scattering of ionization from neon, argon, and xenon in ultrahigh intensities of 2×10^{19} W/cm^2. Comparisons between the gases reveal the energy of the outgoing photoelectron determines its momentum, which can be scattered as far forward as 45° from the laser wave vector k_{laser} for energies greater than 1 MeV. The shell structure in the atom manifests itself as modulations in the photoelectron yield and the width of the angular distributions. We arrive at an agreement with theory by using an independent electron model for the atom, a dipole approximation for the bound state interaction, and a relativistic, three-dimensional, classical radiation field including the laser magnetic field. The studies provide the atomic physics within plasmas, radiation, and particle acceleration in ultrastrong fields.

DOI: 10.1103/PhysRevLett.110.203003 PACS numbers: 32.80.Rm, 33.60.+q, 33.80.Wz

High intensity laser light ($\sim 10^{15}$ W/cm^2) was instrumental for notable advances across disciplines including plasma physics [1], quantum control [2], multielectron ionization and recollision dynamics [3,4], attosecond science [5], molecular dynamics [6], coherent x rays [7], laser fusion [8], and optical science [9]. Laser technology [10] has now advanced to the next generation of ultrahigh intensities ($I \gtrsim 10^{18}$ W/cm^2) where the laser strength parameter $a_0 = E_{\text{laser}}\lambda/(2\pi c^2)$ in atomic units for a field E_{laser} with wavelength λ [11] exceeds 1, and the motion of the electron becomes relativistic within a laser period. In this new regime, particle and photon products exceed a megaelectron volt [11,12]. By rough categorization and factor of ~50 000 in intensity, this represents a progression from what are commonly understood at optical frequencies as perturbative interactions (10^{10} W/cm^2), strong field dynamics (0.5×10^{15} W/cm^2), and now relativistic, ultrastrong field physics (2×10^{19} W/cm^2). The atomic response to ultrahigh laser fields is the initial condition of complex phenomena found in plasmas [13], x-ray generation [14], and laser-based particle acceleration [15]. Ultraintense field-atom measurements serve as a foundation for intensity calibrations of extreme petawatt light sources and provide the needed data for accurate modeling of laser-muon interactions, compact laser accelerators, and laser microcolliders utilizing atomic ionization physics [11].

Here we show atomic ionization at 2×10^{19} W/cm^2 and observe photoelectrons with energies of 1.4 MeV emitted into polar angles 45° from the laser wave vector, k_{laser}. Comparisons between neon, argon, and xenon reveal that the atomic structure, specifically the electron shell binding energy, modifies the photoelectron energy spectra and highest energy cutoff. While highly excited states, rescattering, high harmonic generation, and multielectron processes are known to be prominent in strong fields [16], we find the energy and angle resolved spectra can be described over 3 orders of signal magnitude by a relativistic, independent electron model with classical field scattering and a full nonparaxial treatment of the laser field.

The ultrastrong field-atom interaction may be thought of in two stages: the bound state interaction with ionization and propagation in the continuum including rescattering. We begin by viewing the bound state and ionization process. The high ion charge states [17] interacting with an ultrastrong field (e.g., up to Xe^{26+} in these studies) have binding energies approximately 100 times the optical photon energy ($\hbar\omega$); hence, the bound state can be thought of as responding adiabatically to a quasistatic external field. Ionization adiabaticity is also gauged by an estimated ratio of the tunneling time to the laser period called the Keldysh [18] parameter $\gamma = \omega\sqrt{2IP}/E_{\text{laser}}$ in atomic units for a state with a binding energy (IP). For the ionization of helium (800 nm light at 10^{15} W/cm^2) $\gamma \approx 0.5$, and the response is understood as tunneling since ionization occurs in less than one optical cycle. Atoms in the ultrastrong field are even further into the tunneling regime with γ values of order 0.02 (e.g., Ar^{15+}, 800 nm at 2×10^{19} W/cm^2).

To calculate the initial response of the atom to the ultrastrong field, we use a model based on semiclassical trajectory ensembles. For bound state and ionization calculations, this method is described in Ref. [19]. Briefly, the atom is treated as a single electron, hydrogenlike system. In the calculation, we integrate Newton's equation of motion in 3D, relativistically for 10^5 trajectories. We present the probability distributions for these trajectories as a 3D, x-z color plot integrated over y (E_{laser} is along x and k_{laser} is along z). Figure 1 gives a snapshot of the probability for an electron bound to a $Z = 15$ nucleus ($IP = 855$ eV, angular momentum $\leq 2\hbar$) in the field free case and in an $E_{\text{laser}} = 1.2 \times 10^{11}$ V/cm, $B_{\text{laser}} = 4.1 \times 10^4$ T(2×10^{19} W/cm^2) external field, which is 70% of the critical field where the magnitude of the Coulomb field and E_{laser} are equal for a

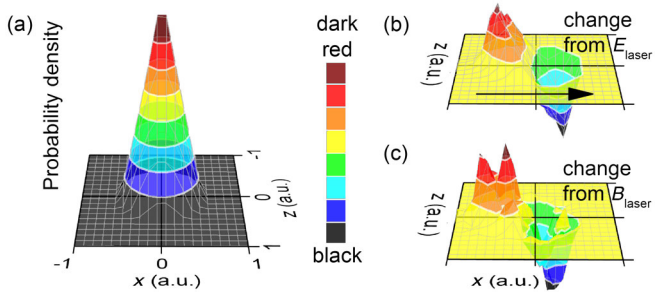

FIG. 1 (color online). Probability density configuration space for an electron bound to Ar^{15+} (a) field free with a color scale from 0 (black) to 1 (dark red). The spatial range shown is ± 1 atomic unit in x and z for (a)–(c). The change due to a 1.2×10^{11} V/cm E_{laser} field (in direction of arrow) is shown in (b) [i.e., the E_{laser} case minus the field free (a)]. The scale is -0.1 (black) to 0.1 (dark red). The probability density difference with full E_{laser} and B_{laser} (4.1×10^4 T along y) fields minus with E_{laser} only is shown in (c) as -0.004 (black) to 0.004 (dark red). A common color scale, black for the smallest values to dark red for the largest values, is used for the figures.

bound state. One can see the peak values for the polarized probability density [Fig. 1(b)]are ~10% of the peak in the unperturbed probability distribution [Fig. 1(a)]. To distinguish any nondipole effects on the bound electron, we show in Fig. 1(c) the difference between the configuration space with the full field and E_{laser} only. The Fig. 1(c) results show the inclusion of B_{laser} changes the bound electron probability density by <1%, primarily as an effective additional shift in the probability density toward the tunneling barrier from the Lorentz force. When considering ionization under these conditions in ultrastrong fields, we again look to clarify the role of B_{laser}. Consistent with the small changes in the bound state (Fig. 1), the calculated classical ionization rates [17,19] at 2×10^{19} W/cm^2 increase by only ~5% with the inclusion of B_{laser}. Hence, ionization can be approximated by tunneling using E_{laser} only. The threshold where B_{laser} in ultrastrong fields may be neglected or must be considered occurs in space approximately at the critical point where E_{laser} equals the Coulomb field. As photoelectrons appear in the continuum near the critical point ($r_{critical} = 4n^2/Z$), we find that including B_{laser} deflects the emerging photoelectron [19] by 2° away from E_{laser} into k_{laser} at 10^{19} W/cm^2. The momentum of the photoelectron appearing in the continuum is a small fraction of the final momentum; thus, the final state emission angle is dominated by the propagation in the laser focus beyond the critical point and here this initial deflection is neglected.

For our studies, the electron final states from Ne, Ar, and Xe ionized by an ultrastrong field were experimentally resolved in energy (ds/dE) and polar angle ($d^2s/dEd\theta$). The measurements are performed with a terawatt, solid-state, ultrafast chirped pulsed amplification laser system [20] that uses microlens pump shaping to achieve a Gaussian spatial mode. The laser emits 150 mJ ($\pm$ 2.9%) pulses with 40 $\pm$ 5 fs duration at 10 Hz repetition rate and 800 nm center wavelength. The prepulse-to-main-pulse ratio is better than 1:10^5. Polarization of the incident beam is altered using a zero-order, quartz $\lambda/4$ wave plate. The peak intensity was confirmed with ion yield measurements to be 2×10^{19} W/cm^2 within an experimental uncertainty range of 0.9×10^{19} W/cm^2 and 2.5×10^{19} W/cm^2. The electron spectrometer [12] consists of an ultrahigh vacuum (UHV) interaction chamber coupled to a magnetic deflection spectrometer (Fig. 2). The UHV chamber is differentially pumped to achieve an ultimate pressure of 10^{-10} torr. In vacuum, the laser is focused to 1.6 μm (FWHM) diameter with an off-axis gold-coated parabola intersecting a skimmed, 10^{11} atoms/cm^3 effusive gas beam with a 0.9 mm half-density width. Photoelectrons are spatially resolved using a slit with an acceptance of 4° in θ prior to entering into the magnetic deflection region. There is no azimuthal dependence since the fields were circularly polarized. The photoelectrons are detected with a scintillator and PMT assembly or microchannel plates. The spectrometer was calibrated with radioactive beta sources, time of flight, and the scintillation photon yield. The spectrometer energy resolution $\triangle E/E$ was 30%. The count rate uncertainty from 200 keV to 1.5 MeV is a factor of $\pm$3, below 200 keV the uncertainty increases to a factor of $\pm$6 due to variations in detection efficiency and gas density across the large focal volume integration. Data points are the average of several independent collections of 10^4 laser shots.

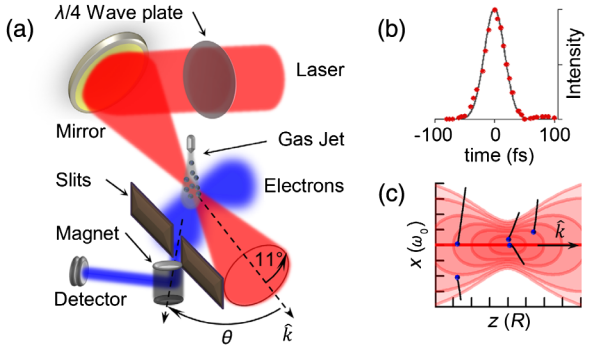

FIG. 2 (color online). Schematic of magnetic deflection spectrometer (a) and laser (red) focused into the sample gas jet (gray). Photoelectrons (blue) are selected by a slit at an angle (θ) and analyzed by magnetic deflection. The time profile of the experimental pulse intensity (circle symbols) and Gaussian (solid line) used in the theory are shown in (b). The focus intensity contours at 0.5, 0.2, 0.1, 0.05, 0.02, and 0.01 times the peak intensity are in (c). The tick marks along z are in units of the Raleigh range ($R = 7.2$ μm) and along x in units of the beam waist ($\omega_0 = 1.35$ μm). Sample electron trajectories are shown (solid lines) calculated at (x, y, z) = (0, 0.5 μm, 0), (0, 0, 0.5 μm), (-3 μm, 0, 20 μm), (1 μm, 0, 10 μm), and (-1.5 μm, 0, -20 μm) over the time periods (initial, final) = (-2.5 fs, 14.5 fs), (-2.5 fs, 20 fs), (-60 fs, -30 fs), (-100 fs, 30 fs), and (-60 fs, -5 fs), respectively.

The experimental energy spectra shown in Fig. 3 reveal photoelectrons with energies from 50 keV up to a cutoff energy of 1.4 MeV for Ar and Xe, and 500 keV for Ne. The spectra for Ar and Xe both have modulations as a function of energy. The most prominent of these is the suppression in the Ar yield at 200 keV. Since the laser is identical for Ne, Ar, and Xe, the cutoff energy and modulation in the spectra reflect atomic structure. Calculations of the continuum dynamics and photoelectron final states (Figs. 3 and 4) are described in Ref. [21]. Tunneling is treated with the instantaneous electric field across a 40 fs pulse [Fig. 2(b)]. Starting with the neutral atom, the ionization is evaluated sequentially with respect to increasing charge using classical trajectory ensembles (weighted by the tunneling probability) to simulate the continuum photoelectron. The electron energy at the time of its birth or appearance in the continuum is set to be zero. The results are spatially integrated from the center of the focus out to the points in the focus where the peak intensity is 2×10^{17} W/cm^2. Comparisons to the experimental results (Fig. 3) used a 30% energy resolution and 4° θ convolution. The calculated ion populations as a function of time are shown in Fig. 4(a). As the laser pulse [Fig. 2(b)] is increasing to its maximum intensity, deeper and deeper bound states are sequentially removed as the laser sweeps across the Coulomb field binding the electron. For Ne, the $n = 2$ valence shell is removed well before the peak of the pulse. The final ion state is Ne^{8+} since 10^{19} W/cm^2 is insufficient to ionize the $1s$ electron ($IP = 1362$ eV). For Ar, early in the pulse the $n = 3$ shell (Ar to Ar^{8+}) ionizes and then nearer to the peak of the pulse the $n = 2$ shell (Ar^{9+} to Ar^{16+}). Xe ionization begins with the $5p$ electron ($IP = 12$ eV) and proceeds through the pulse until reaching Xe^{26+}. Contrasting with traditional strong fields, where photoionization is viewed as a "stepwise" process involving one- or two-electron ionizing during the pulse and appearing distinctly in the continuum [22], ultrastrong fields involve many charge states and photoionization becomes essentially continuous for electrons removed from an atomic shell. Between shells, such as the $n = 2$, 3 in Ar, ionization shuts off as can be seen in the stagnant Ar^{8+} yield 40 fs before the peak of the pulse [Fig. 4(a)]. Consequently, there is a reduction in electrons with energies produced at that field strength. For Ar, this is manifested as the dip in the yield at 200 keV [Fig. 3(d)]. For Ne, ionization shuts off after the $n = 2$ shell, explaining the simple structure in the measured and calculated yield [Fig. 3(b)] and lack of photoelectrons at the highest MeV energies. For Xe, the modulation in the ionization yield is less striking since there is a lack of distinction between the $n = 4$ and $n = 5$ electron shells (due to the energy shift of the $4d$ electrons) and ionization is only briefly interrupted (Xe^{8+}, Xe^{18+}) during the rise in the laser pulse.

As the electron velocity is driven relativistically by E_{laser}, the photoelectron is deflected by the Lorentz force into the

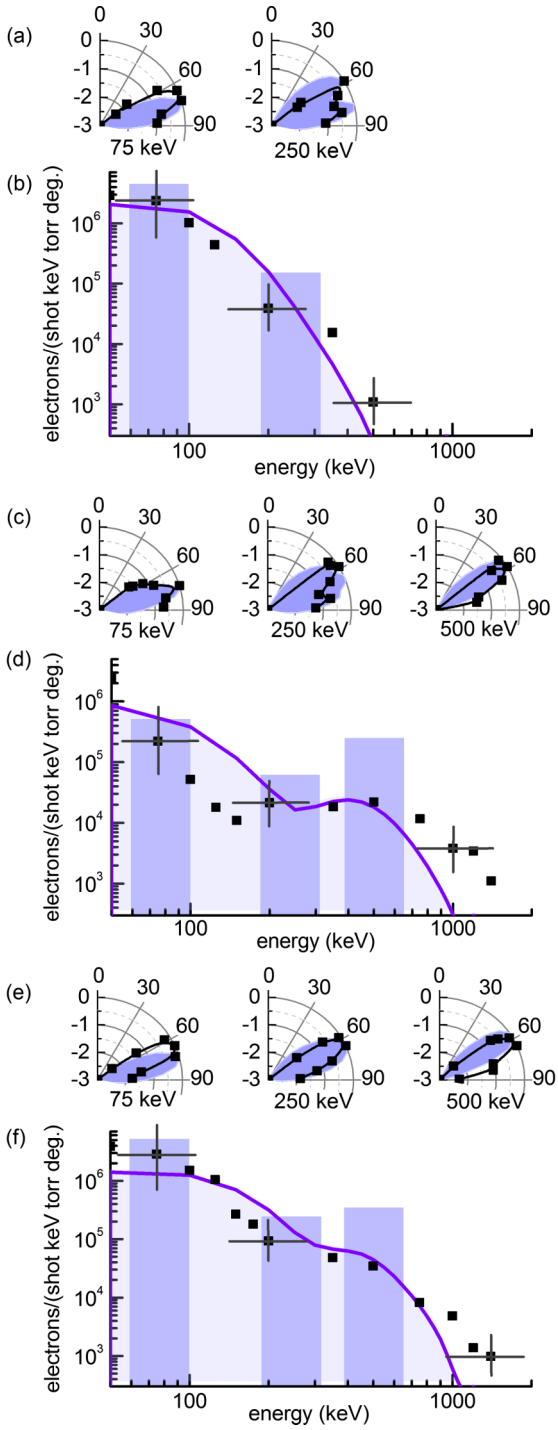

FIG. 3 (color online). Photoelectron energy spectra (PES) for $\theta = 72°$ with AERPES at 2×10^{19} W/cm^2. AERPES for Ne (a) at 75 and 250 keV and the PES (b). AERPES for Ar (c) at 75, 250, and 500 keV and the PES for Ar (d). AERPES for Xe (e) at 75, 250, and 500 keV and PES (f). Radial values in AERPES polar plots are on a normalized Log_{10} scale from 0 to −3, i.e., 3 orders of signal magnitude. AERPES measurements are shown (square symbols) with a fit to aid the eye. Calculations are shown (solid line) in (b, d, f) and (fill) in (a, c, e). PES (square symbols) include representative error bars. Shaded rectangles indicate where AERPES collections are taken. The bar height (b, d, f) is the angle integrated yield (electrons/shot keV torr) at that energy.

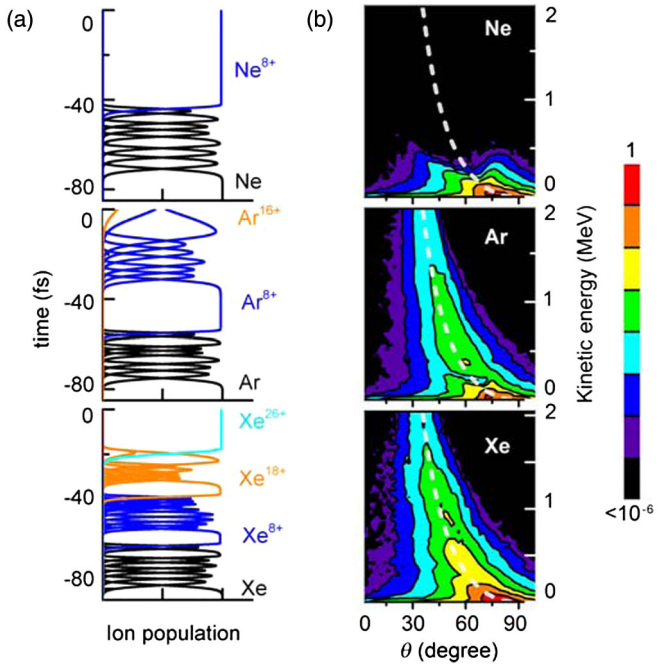

FIG. 4 (color online). Calculated time resolved ion populations (a) before the peak of the laser pulse (0 fs) with (b) the calculated energy, angle resolved photoelectron yields for 2×10^{19} W/cm^2. Slices from the energy, angle resolved photoelectron yield at 75, 250, and 500 keV convoluted with the experimental resolution are shown in Figs. 3(a), 3(c), and 3(e). The superimposed dashed line is the plane wave solution. The logarithmic color scale in (b) ranges from red (1) to black ($< 10^{-6}$).

laser propagation direction [Fig. 2(c)] since $E_{\text{laser}} \times B_{\text{laser}}$ is along k_{laser}. The effect of the Lorentz force can be seen in the polar angle, energy resolved photoelectron spectra (AERPES) of Figs. 3(a), 3(c), and 3(e). The measured values (mean ± standard deviation) at 75 keV are 75° ± 6°, 79° ± 7°, and 72° ± 6° for Ne, Ar, and Xe, respectively, and at 500 keV are 63° ± 7° and 67° ± 7° for Ar and Xe, respectively. The simple relationship between the electron energy and forward deflected angle in a plane wave is significantly modified by the curvature of the focus wave front [23]. In our experiments the irradiance contour asymptote of the focus (Fig. 2) approaches a cone angle of $\theta = (\lambda/\pi w_0) = 11°$, where w_0 is the exp(−2) irradiance radius at the focus. The agreement with the calculated angular distributions [also shown in Figs. 3(a), 3(c), and 3(e)] indicates the width in the emission angle is a result of the angular range of k_{laser} across the outgoing wave front, and the mean polar angle is primarily a function of the emitted photoelectron energy (the mean emission angles at 75 keV, for example, are all within the measurement accuracy). A comparison between the calculated energy, angle resolved yield with a plane wave, and the experimental focus is shown in Fig. 4(b). Broader polar angular distributions (e.g., Ar at 250 keV) occur when the emission at that angle is suppressed and contributions to the yield are coming from ionization prior to or after the intensity that would normally create electrons at that energy.

The model showed a similar sensitivity to the experimental signal range. Changes in time-dependent ionization [Fig. 4(a)] much greater than 10^{-3} of the peak value visibly modify the yields reported in Fig. 3. Multiply populated fine-structure states, highly excited states, and multielectron interactions are known to occur in strong field ionization. We find these processes do not lead to a disagreement with the electron yields expected using an independent, sequential ionization model. The result can be interpreted to mean the integrated yields of the ion population from these processes (including rescattering) is at the level of 10^{-3} compared to the independent electron processes. More likely, however, they are prominent in ultrastrong fields, especially high-Z species like Xe, but are highly correlated with the one-electron processes and occur on attosecond to few femtosecond times scales. As a result, they "follow" the sequential ion populations (Fig. 4) and energy, angle resolved yields. In the future, classical and quantum calculations should be able to shed additional light on the important role of the excitation and multielectron dynamics in ultrastrong fields [24].

Atomic ionization in ultrastrong fields gains new dynamics from the role of the B_{laser}, relativistic motion, extended laser focus, and a change in the role of atomic structure from individual electrons towards the electron shell structure. AERPES are measured as far as 45° into k_{laser} at 10^{19} W/cm^2 for final energies greater than a megaelectron volt. While multielectron effects, collisional excitation, high harmonic radiation, and highly excited states, for example, are certain to play a role in the dynamics, agreement with the energy and angle resolved data may be obtained with an independent electron model with classical field scattering and a full nonparaxial E_{laser}, B_{laser} treatment of the field.

This material is based upon work supported by the Army Research Office under Grant No. W911NF-09-1-0390 and the National Science Foundation under Grant No. 0757953.

[1] W. P. Leemans, B. Nagler, A. J. Gonsalves, C. Toth, K. Nakamura, C. G. R. Geddes, E. Esarey, C. B. Schroeder, and S. M. Hooker, Nat. Phys. **2**, 696 (2006).
[2] R. Levis, G. Menkir, and H. Rabitz, Science **292**, 709 (2001).
[3] A. N. Pfeiffer, C. Cirelli, M. Smolarski, R. Doerner, and U. Keller, Nat. Phys. **7**, 428 (2011).
[4] A. D. Shiner, B. E. Schmidt, C. Trallero-Herrero, H. J. Woerner, S. Patchkovskii, P. B. Corkum, J.-C. Kieffer, F. Legare, and D. M. Villeneuve, Nat. Phys. **7**, 464 (2011).
[5] P. Paul, E. Toma, P. Breger, G. Mullot, F. Auge, P. Balcou, H. Muller, and P. Agostini, Science **292**, 1689 (2001).
[6] S. Baker, J. Robinson, C. Haworth, H. Teng, R. Smith, C. Chirila, M. Lein, J. Tisch, and J. Marangos, Science **312**, 424 (2006).

[7] T. Popmintchev, M.-C. Chen, D. Popmintchev, P. Arpin, S. Brown, S. Alisauskas, G. Andriukaitis, T. Balciunas, O. D. Muecke, A. Pugzlys, A. Baltuska, B. Shim, S. E. Schrauth, A. Gaeta, C. Hernandez-Garcia, L. Plaja, A. Becker, A. Jaron-Becker, M. M. Murnane, and H. C. Kapteyn, Science **336**, 1287 (2012).
[8] S. H. Glenzer *et al.*, Science **327**, 1228 (2010).
[9] C. Thaury, F. Quere, J.-P. Geindre, A. Levy, T. Ceccotti, P. Monot, M. Bougeard, F. Reau, P. D'Oliveira, P. Audebert, R. Marjoribanks, and P. H. Martin, Nat. Phys. **3**, 424 (2007).
[10] B. Walker, C. Toth, D. Fittinghoff, T. Guo, D. Kim, C. Rose-Petruck, J. Squier, K. Yamakawa, K. Wilson, and C. Barty, Opt. Express **5**, 196 (1999).
[11] A. Di Piazza, C. Mueller, K. Z. Hatsagortsyan, and C. H. Keitel, Rev. Mod. Phys. **84**, 1177 (2012).
[12] A. D. DiChiara, I. Ghebregziabher, R. Sauer, J. Waesche, S. Palaniyappan, B. L. Wen, and B. C. Walker, Phys. Rev. Lett. **101**, 173002 (2008).
[13] J. Faure, C. Rechatin, A. Norlin, A. Lifschitz, Y. Glinec, and V. Malka, Nature (London) **444**, 737 (2006).
[14] A. Rousse, K. Phuoc, R. Shah, A. Pukhov, E. Lefebvre, V. Malka, S. Kiselev, F. Burgy, J. Rousseau, D. Umstadter, and D. Hulin, Phys. Rev. Lett. **93**, 135005 (2004).
[15] X. Wang, R. Zgadzaj, S. A. Yi, V. Khudik, W. Henderson, N. Fazel, Y.-Y. Chang, R. Korzekwa, H.-E. Tsai, C.-H. Pai, Z. Li, E. Gaul, M. Martinez, G. Dyer, H. Quevedo, A. Bernstein, M. Donovan, G. Shvets, T. Ditmire, and M. C. Downer, J. Plasma Phys. **78**, 413 (2012).
[16] L. F. DiMauro and P. Agostini, Adv. At. Mol. Opt. Phys. **35**, 79 (1995).
[17] H. G. Hetzheim and C. H. Keitel, Phys. Rev. Lett. **102**, 083003 (2009).
[18] P. Colosimo, G. Doumy, C. I. Blaga, J. Wheeler, C. Hauri, F. Catoire, J. Tate, R. Chirla, A. M. March, G. G. Paulus, H. G. Muller, P. Agostini, and L. F. Dimauro, Nat. Phys. **4**, 386 (2008).
[19] P. D. Grugan, S. Luo, M. Videtto, C. Mancuso, and B. C. Walker, Phys. Rev. A **85**, 053407 (2012).
[20] A. DiChiara, E. Chowdhury, G. Ongadi, B. Walker, and R. Tamosaitis, Opt. Lett. **28**, 2106 (2003).
[21] E. Chowdhury, I. Ghebregziabher, J. MacDonald, and B. Walker, Opt. Express **12**, 3911 (2004).
[22] P. B. Corkum, Phys. Rev. Lett. **71**, 1994 (1993).
[23] S. X. Hu and A. F. Starace, Phys. Rev. E **73**, 066502 (2006).
[24] P. Ho, R. Panfili, S. Haan, and J. Eberly, Phys. Rev. Lett. **94**, 093002 (2005).